

Cite this: *Dalton Trans.*, 2024, **53**,
8168

Defect engineering of a TiO₂ anatase/rutile homojunction accelerating sulfur redox kinetics for high-performance Na–S batteries†

Yue Xiao,^a Yelei Zheng,^a Ge Yao,^{*a} Yuhang Zhang,^a Zhiqiang Li,^a Shoujie Liu^{*a} and Fangcai Zheng ^{*a,b}

Room-temperature sodium–sulfur (RT Na–S) batteries have the drawbacks of the poor shuttle effect of soluble sodium polysulfides (NaPSs) as well as slow sulfur redox kinetics, which result in poor cycling stability and low capacity, seriously affecting their extensive application. Herein, defect engineering is applied to construct rich oxygen vacancies at the interface of a TiO₂ anatase/rutile homojunction (O_V-TRA) to enhance sulfur affinity and redox reaction kinetics. Combining structural characterizations with electrochemical analysis reveals that O_V-TRA well alleviates the shuttle effect of NaPSs and precipitates the deposition and diffusion kinetics of Na₂S. Consequently, S/O_V-TRA provides excellent electrochemical performance with a reversible capacity of 870 mA h g⁻¹ at 0.1 C after 100 cycles and a long-term cycling capability of 759 mA h g⁻¹ at 1 C after 1000 cycles. This work provides an effective interfacial defect engineering strategy to promote the application of metal oxides in RT Na–S batteries.

Received 12th March 2024,
Accepted 15th April 2024

DOI: 10.1039/d4dt00745j

rsc.li/dalton

1. Introduction

Room-temperature sodium–sulfur (RT Na–S) batteries are considered an attractive alternative for next-generation energy storage systems owing to their high theoretical energy density (1274 W h kg⁻¹) and low cost.^{1–3} Furthermore, RT Na–S batteries have a wide range of large-scale market application prospects owing to abundant Na and S resources.^{4,5} Nevertheless, RT Na–S batteries suffer from sluggish kinetics, which results in the diffusion of long-chain sodium polysulfides (NaPSs) into the electrolyte and further leads to a series of more serious problems, including low battery capacity, rapid capacity decay, enormous volume change, quick structural collapse and low utilization efficiency of active S components.^{6–9} These disappointing results are also related to the insulation characteristics of S and Na₂S₂/Na₂S.¹⁰ Therefore, it is crucial to design a host material that not only enhances the electronic conductivity of S, but also immobilizes soluble NaPSs and

accelerates their reversible transformation into a fully discharged product of Na₂S.

A variety of strategies are designed to fabricate advanced S host materials for RT Na–S batteries. Carbon-based materials with large specific surface areas, including carbon spheres,^{11,12} carbon nanotubes,^{13,14} and microporous carbon skeletons,^{15–17} are popular S host materials to improve electronic conductivity and alleviate volume expansion. For example, Wu *et al.* synthesized carbon spheres with continuous pore distribution to alleviate the volume expansion of S and Na₂S₂/Na₂S for RT Na–S batteries.¹⁸ However, the weak physical interaction between the nonpolar carbon matrix and polar NaPSs makes it difficult to effectively suppress NaPSs diffusion, leading to the unfavorable shuttle effect and abysmal capacity decay.¹⁹ To obtain a superior S cathode, polar materials with strong polar–polar interaction toward NaPSs are proposed, such as oxides,^{20,21} sulfides,^{22,23} and transition metal nanoclusters/single atoms,^{24–28} where a strong polar chemical interaction is conducive to anchor NaPSs and catalyze their rapid conversion, which is critical to suppress the shuttle effect and improve the cycling stability of the S cathode. Li *et al.* reported that Y single-atom catalysts with a Y–N₄ structure were beneficial for the chemical affinity of NaPSs and lowered the conversion kinetics.²⁹ Mou *et al.* prepared a highly efficient MoC@NHC electrocatalyst to alleviate volume change and suppress the diffusion of polysulfides.³⁰ However, it is difficult to precisely control the catalyst structure at the atomic level. In contrast, oxygen vacancy engineering is

^aInstitutes of Physical Science and Information Technology, School of Materials Science and Engineering, Key Laboratory of Structure and Functional Regulation of Hybrid Materials, Anhui University, Hefei, Anhui 230601, China.

E-mail: zfc@mail.ustc.edu.cn, jiesliu@ahnu.edu.cn, anne_yao1995@163.com

^bHigh Magnetic Field Laboratory, Hefei Institutes of Physical Science, Chinese Academy of Sciences, Hefei, Anhui, 230031, P. R. China.

E-mail: zfc@mail.ustc.edu.cn

† Electronic supplementary information (ESI) available. See DOI: <https://doi.org/10.1039/d4dt00745j>

one of the most effective strategies to anchor LiPSs and accelerate their conversion in Li-S batteries owing to the fact that an oxygen vacancy site can strongly accommodate electrons from LiPSs and thus accelerate reaction kinetics.^{31,32} Zou *et al.* reported that the oxygen vacancy in the structure of $\text{In}_2\text{O}_{3-x}$ facilitated the strong interaction toward LiPSs and accelerated the S redox kinetics.³³ Based on the above analysis, constructing a defect structure with abundant oxygen vacancies could be also an effective strategy to accelerate S redox kinetics in RT Na-S batteries.

The formation of oxygen vacancy is closely related to interfacial band structures, such as heterostructures and homogeneous structures, which are beneficial for promoting charge transfer and encouraging catalytic activity.^{34–36} Interestingly, compared with heterojunction, homojunction promotes faster charge transfer and has strong electron conductivity due to ideal interfacial contact and near-perfect lattice mismatching.^{37,38} Therefore, constructing oxygen vacancy at the interface of the homojunction structure possesses the superiority in generating much more active sites to adsorb S species. However, it is rare to design a homogeneous structure for capturing NaPSs and boosting their conversion in RT Na-S batteries. As one of the typical metal oxides, TiO_2 delivers high adsorption for polysulfides based on strong Lewis acid–base interaction between Ti^{4+} and the electron-rich S_x^{2-} , but the low electrical conductivity intrinsically limits the conversion efficiency of S.^{39,40} Particularly, the formation of surface phase junctions between anatase and rutile always easily introduces abundant oxygen vacancies, which can promote the interaction toward reaction intermediates and lower the reaction barrier.⁴¹

In this work, we constructed abundant oxygen vacancies at the interface of anatase and rutile through thermal calcination of $\text{NH}_2\text{-MIL-125(Ti)}$. Besides, owing to the carbonization of organic linkers during the calcination process, the resulting oxygen-vacancy-rich TiO_2 homojunction structure is well dispersed into the carbon skeleton (denoted as $\text{O}_V\text{-TRA}$). The physical characterization data confirmed that the homojunction structure facilitates the formation of oxygen vacancy. Moreover, the electrochemical analysis demonstrates that the oxygen vacancy is beneficial for the adsorption of NaPSs and promotes the reaction kinetics. The resulting S/ $\text{O}_V\text{-TRA}$ displays enhanced electrochemical performance for RT Na-S batteries with a long cycling lifespan, excellent rate capability, and high coulombic efficiency.

2. Results and discussion

The schematic diagram illustrates the fabrication procedures of $\text{O}_V\text{-TRA}$ *via* calcining $\text{NH}_2\text{-MIL-125(Ti)}$ in Ar (Fig. 1a). Notably, the anatase TiO_2 is metastable and can be converted into the rutile TiO_2 at high temperatures. The transformation process usually introduces abundant defects at the interface, which is beneficial for increasing the conductivity of the material.⁴¹ The X-ray powder diffraction (XRD) pattern of the resulting precursor is well indexed to $\text{NH}_2\text{-MIL-125(Ti)}$

(Fig. S1†), and the scanning electron microscopy (SEM) image (Fig. 1b) reveals that $\text{NH}_2\text{-MIL-125(Ti)}$ exhibits a uniform circular-cake structure with a diameter of 400–500 nm and thickness of 200 nm. After calcination at 550 °C, $\text{NH}_2\text{-MIL-125(Ti)}$ was decomposed into oxygen-vacancy-rich anatase TiO_2 within an N-doped carbon skeleton (recorded as $\text{O}_V\text{-TA}$). $\text{O}_V\text{-TA}$ still maintains the mooncake-like morphology (Fig. S2†). As the pyrolysis temperature increases, some metastable $\text{O}_V\text{-TA}$ is transformed progressively into crystalline rutile TiO_2 .⁴² Thus, $\text{O}_V\text{-TRA}$ was formed at 800 °C. Fig. 1c and d displays SEM and transmission electron microscopy (TEM) images of $\text{O}_V\text{-TRA}$, which maintains a similar mooncake-like structure. Significantly, the surface of $\text{O}_V\text{-TRA}$ is crude, where small particles agglomerate on the surface of the mooncake, suggesting that the high temperature facilitates the transformation of $\text{NH}_2\text{-MIL-125(Ti)}$ into large-sized TiO_2 nanoparticles.⁴³ The high-resolution transmission electron microscopy (HRTEM) and inverse fast Fourier transform (IFFT) images show lattice fringe spacings of 0.231 and 0.170 nm (Fig. 1e and f), corresponding to the (004) plane of anatase and (211) plane of rutile, respectively, achieving the anatase-rutile homogeneous structure. The selected area electron diffraction (SAED) image in Fig. 1g can be attributed to the planes of anatase ((101) and (004)) and rutile ((110) and (211)), further manifesting the formation of anatase-rutile homojunction in $\text{O}_V\text{-TRA}$. The interface of anatase-rutile TiO_2 homojunction is beneficial for smooth electron migration.⁴⁴ Furthermore, the homojunction is organized within a conductive N-doped carbon network from the carbonization of the organic ligand in $\text{NH}_2\text{-MIL-125(Ti)}$.⁴¹ As shown in Fig. 1h–k, energy-dispersive X-ray spectroscopy (EDX) mapping images indicate the uniform distribution of C, N, O, and Ti across $\text{O}_V\text{-TRA}$, indicating an evenly dispersed anatase-rutile homogeneous structure. Besides, TRA without oxygen vacancy was also prepared to explore the positive effect of oxygen vacancy on the electrochemical performance of RT Na-S batteries, and it shows a similar morphology with $\text{O}_V\text{-TRA}$ (Fig. S3†).

The XRD pattern (Fig. 2a) displays that the peaks of $\text{O}_V\text{-TRA}$ are indexed to anatase TiO_2 (No. 89-4921) and rutile TiO_2 (No. 21-1276), demonstrating the formation of a homojunction. Besides, the generation of $\text{O}_V\text{-TA}$ at low calcination temperature is also confirmed. After the removal of oxygen vacancy, the homojunction is still retained. X-ray photoelectron spectroscopy (XPS) was performed to further explore the elemental chemical states of $\text{O}_V\text{-TRA}$. Fig. 2b shows the signals of Ti, O, C, and N elements in the full survey of $\text{O}_V\text{-TRA}$. The Ti 2p spectrum for $\text{O}_V\text{-TRA}$ shows an obvious peak of Ti^{3+} compared to those of TRA and $\text{O}_V\text{-TA}$ (Fig. 2c). More importantly, the ratio of $\text{Ti}^{4+}/\text{Ti}^{3+}$ is 2.70 for $\text{O}_V\text{-TRA}$, which is lower than that in $\text{O}_V\text{-TA}$ (2.82), signifying the formation of structural defects and contributing to the existence of more oxygen vacancies.⁴⁴ In the Ti 2p spectrum of $\text{O}_V\text{-TRA}$ (located at 464.99 eV and 459.32 eV), the binding energy of Ti^{4+} shifts negatively by 0.05 eV compared to that in TRA (located at 465.04 eV and 459.37 eV), indicating that $\text{O}_V\text{-TRA}$ owns a higher electron density at the Ti site. This can imply the high electron-attracting impression,

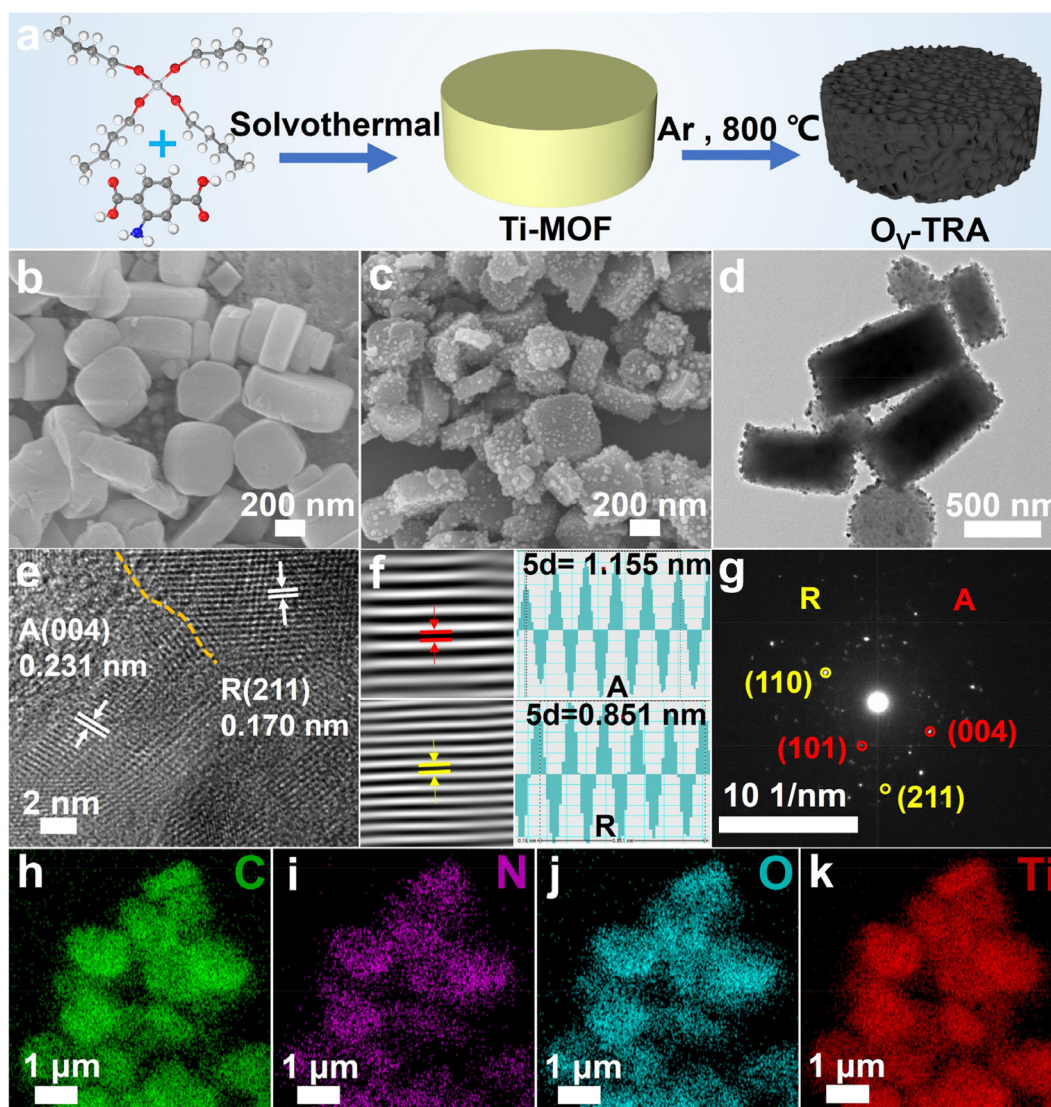


Fig. 1 (a) Schematic of the preparation procedure for O_V -TRA. SEM images of (b) NH_2 -MIL-125(Ti) and (c) O_V -TRA. (d) TEM and (e) HRTEM images of O_V -TRA. (f) The corresponding inverse fast Fourier transform (IFFT) lattice fringes. (g) SAED pattern of O_V -TRA. (h–k) EDS mapping images of corresponding elements in O_V -TRA.

and prove the existence of oxygen vacancy.⁴⁵ The O 1s spectra for O_V -TRA and O_V -TA, as shown in Fig. S4,[†] display three peaks, which are attributed to lattice oxygen (O_L), oxygen vacancy (O_V), and surface hydroxyl (O_C).⁴⁶ Compared to TRA (530.67 eV) and O_V -TA (530.27 eV), the O 1s peak of O_V -TRA (530.75 eV) shifts to a higher binding energy region, thereby confirming the existence of oxygen vacancy in O_V -TRA.⁴⁷ More convincingly, the concentration of O_V in O_V -TRA is 22.74%, which is higher than that of O_V -TA (11.59%), indicating the palpable lattice defects in O_V -TRA. To better distinguish the valence and differences in the chemical environment of Ti in O_V -TRA and TRA, X-ray absorption near edge structure (XANES) spectra at Ti K-edge were measured.⁴⁵ Fig. 2d reveals the XANES spectra of O_V -TRA and TRA with Ti foil as a reference. The absorption edge of O_V -TRA shifts negatively com-

pared to TRA, verifying that Ti in O_V -TRA has higher electron charge and a lower valence state compared to TRA.⁴⁸ This result is the same as the results of XPS. Furthermore, as displayed in Fig. S5,[†] the Fourier transform (FT) k^3 -weighted extended X-ray absorption fine structure (EXAFS) spectra of O_V -TRA and TRA exhibit the peaks at ≈ 1.5 Å and ≈ 2.5 Å, which correspond to Ti–O bond and Ti–Ti bond, respectively.^{49,50} These results further confirm that the oxygen vacancy can induce the localized electron distribution on Ti sites in O_V -TRA, which can enhance the sulfur affinity and redox reaction kinetics. The electron paramagnetic resonance (EPR) was performed to further verify the defects of the oxygen vacancy (Fig. 2e). A g value of 1.998 refers to oxygen defects in O_V -TRA and O_V -TA, where O_V -TRA has the stronger signal than O_V -TA, indicating the existence of defects in O_V -TRA, which is attribu-

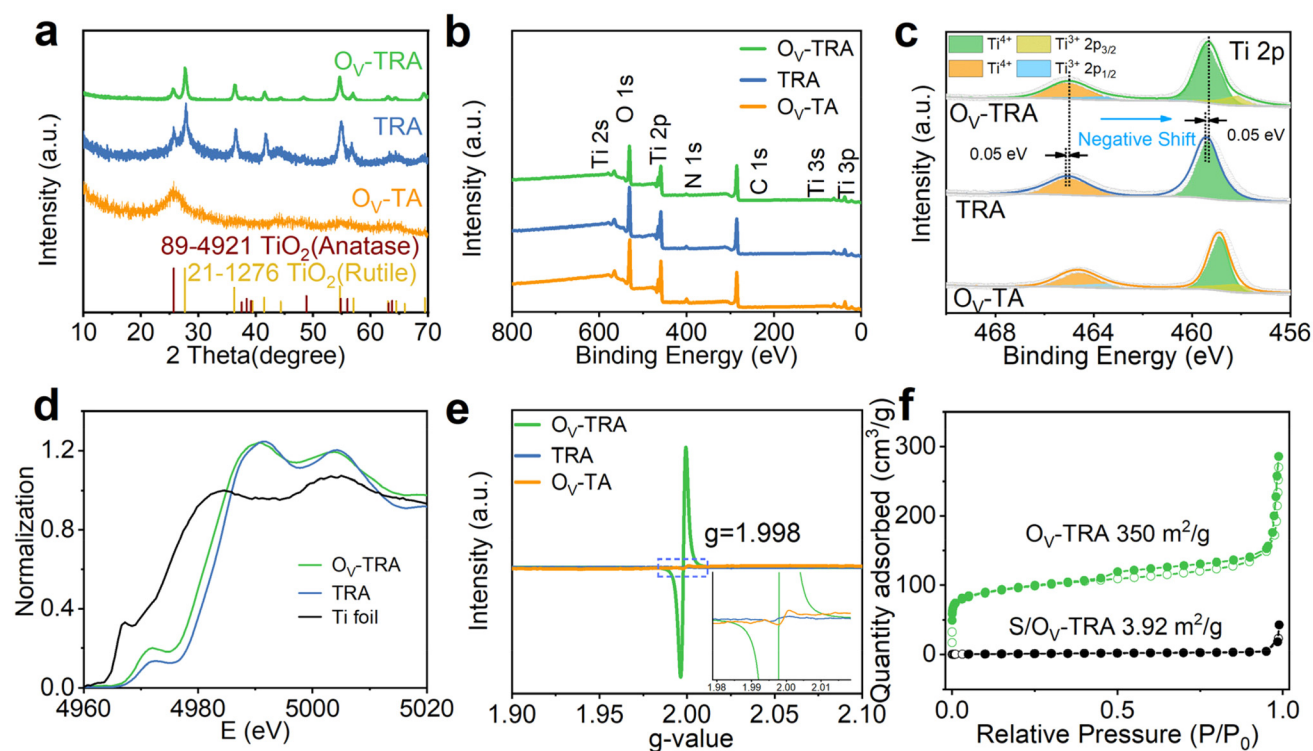


Fig. 2 (a) XRD patterns and (b) the full survey XPS spectra and (c) Ti 2p spectra of O_V -TRA, O_V -TA and TRA. (d) Ti K-edge XANES spectra of O_V -TRA, TRA and Ti foil. (e) EPR spectra of O_V -TRA, O_V -TA and TRA. (f) N_2 adsorption–desorption isotherms of O_V -TRA and S/ O_V -TRA.

ted to incompatible interface between anatase and rutile phases.⁵¹ It is worth noting that TRA shows almost no sign of oxygen defects. The interface of the anatase-rutile TiO_2 homo-junction is beneficial for smooth electron migration. These results also agree well with the XPS analysis, and the obtained homojunction with abundant oxygen vacancies is beneficial to upgrade the intrinsic electrical conductivity.³³ Furthermore, the defects induced by oxygen vacancies enhance the wide-range adsorption capacity towards electron-rich polysulfides, serving as catalytic sites to promote the transformation of polysulfides.⁵²

The prepared samples serve as S hosts for RT Na–S batteries, which are correspondingly recorded as S/ O_V -TRA, S/TRA and S/ O_V -TA. They still maintain the mooncake-like morphology based on SEM and TEM images (Fig. S6†). XRD patterns confirmed the successful loading of S into the host materials (Fig. S7†) and the S content in S/ O_V -TRA, S/TRA and S/ O_V -TA was 56.20, 49.41 and 49.11 wt%, respectively (Fig. S8†). The increased S content in O_V -TRA further certifies that the rich oxygen vacancies facilitate the immobilization of S_8 . The specific surface area of O_V -TRA was analyzed as $350\text{ m}^2\text{ g}^{-1}$ (Fig. 2f), which is higher than that of O_V -TA ($112\text{ m}^2\text{ g}^{-1}$) and TRA ($318\text{ m}^2\text{ g}^{-1}$) (Fig. S10a, S11a, and Table S1†). The pore volume of O_V -TRA ($0.419\text{ cm}^3\text{ g}^{-1}$) is higher than those of O_V -TA ($0.418\text{ cm}^3\text{ g}^{-1}$) and TRA ($0.409\text{ cm}^3\text{ g}^{-1}$) (Fig. S9, S10b and S11b and Table S2†). The exceptional specific surface area and pore volume of O_V -TRA generously provide many more sites for

loading S, adequately enhancing the contact area between the electrolyte and the electrode material. S/ O_V -TRA shows the reduced specific surface area ($3.92\text{ m}^2\text{ g}^{-1}$) and pore volume ($0.066\text{ cm}^3\text{ g}^{-1}$) compared to those of O_V -TRA, demonstrating the successful and uniform storage of S in their defective structure. Likewise, S/ O_V -TA ($4.26\text{ m}^2\text{ g}^{-1}$ and $0.392\text{ cm}^3\text{ g}^{-1}$) and S/TRA ($15.11\text{ cm}^3\text{ g}^{-1}$ and $0.073\text{ cm}^3\text{ g}^{-1}$) reveal reduced specific surface area and pore volume after the introduction of S. These results demonstrate that S was successfully melted into the host materials.

The visualized adsorption experiment was carried out to further verify the adsorption ability of O_V -TRA toward Na_2S_6 . As shown in Fig. 3a, identical masses of O_V -TRA, O_V -TA and TRA were immersed into Na_2S_6 solution (FEC/PC, 1:1 by volume). O_V -TRA made the color of the solution change from vibrant yellow to nearly colorless after 12 h, whereas O_V -TA and TRA only made the color pale yellow. Moreover, the supernatant of the adsorbed solution was further tested by ultra-violet-visible spectroscopy (UV-vis) (Fig. 3b), and the peak around 300 nm corresponds to the S_6^{2-} species. Furthermore, the peak of S_6^{2-} is lower than those of O_V -TA and TRA, confirming the stronger adsorption ability of O_V -TRA for Na_2S_6 . These outcomes demonstrate the favorable chemical adsorption and anchoring capacity of O_V -TRA toward NaPSs, which contributes to suppressing the diffusion of NaPSs into the electrolyte. Simultaneously, XPS was further conducted to explore the underlying interaction between O_V -TRA and Na_2S_6 .

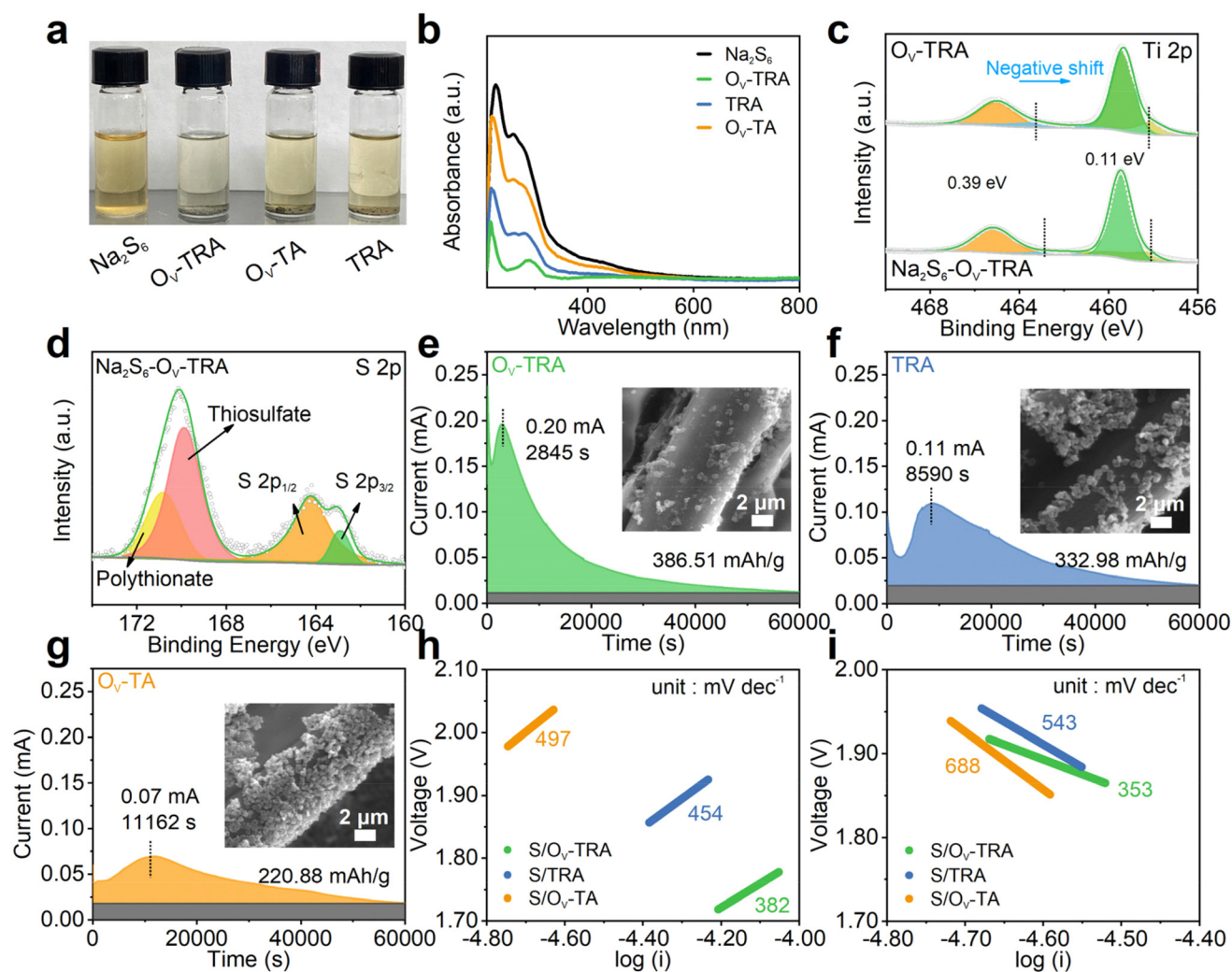


Fig. 3 (a) Digital images of O_V -TRA, O_V -TA, and TRA immersed into Na_2S_6 -PC/FEC. (b) UV-vis spectra of O_V -TRA, O_V -TA, and TRA. (c and d) XPS profiles of Ti 2p and S 2p of O_V -TRA after interacting with Na_2S_6 solution. (e–g) Potentiostatic discharge curves (Na_2S_6) of O_V -TRA, TRA and O_V -TA. (h) Tafel plots calculated from oxidation peaks. (i) Tafel plots calculated from reduction peaks.

The peaks of Ti 2p_{3/2} and Ti 2p_{1/2} negatively shift (Fig. 3c), which is attributed to the electron transfer from Na_2S_6 to O_V -TRA,⁵³ revealing the increased electron density located at oxygen vacancy and strong chemical interaction. Besides, the S 2p spectra at 169.96 and 170.91 eV (Fig. 3d) can be attributed to thiosulfate and polythionate, and the two peaks at around 164 eV can be attributed to S 2p_{1/2} and S 2p_{3/2}. The formation of thiosulfate and polythionate demonstrates the oxidation of NaPSSs by O_V -TRA.⁵⁴ Likewise, the experiments were repeated with 1,2-dimethoxyethane (DME), and O_V -TRA still exhibited enhanced adsorption ability toward Na_2S_6 (Fig. S12[†]). The XPS results also confirmed that the peaks of Ti 2p_{3/2} and Ti 2p_{1/2} negatively shifted (Fig. S13[†]), which is attributed to the electron transfer from Na_2S_6 to O_V -TRA, revealing the increased electron density located at oxygen vacancy and strong chemical interaction. Furthermore, potentiostatic nucleation and growth experiments (Fig. 3e–g and Fig. S14[†]) were carried out at 1.25 V to further investigate the catalytic effect on the polysulfide

conversion. The deposition of Na_2S on O_V -TRA is significantly faster (2845 s) at a larger current response (0.20 mA) than those of O_V -TA (8590 s, 0.11 mA) and TRA (11162 s, 0.07 mA). In addition, O_V -TRA delivers the highest deposition capacity of 386.51 mA h g⁻¹ compared with that of O_V -TA (332.98 mA h g⁻¹) and TRA (220.88 mA h g⁻¹). The findings show that the high-density oxygen vacancies in O_V -TRA exhibit excellent adsorption capacity towards NaPSSs, and endow the higher electrochemical activity toward Na_2S precipitation, which contributes to inhibit the shuttle effect and promote the conversion of NaPSSs. The Tafel slope (Fig. S15[†]) from the oxidation peak (Fig. 3h) of S/ O_V -TRA (382 mV dec⁻¹) is inferior to those of S/ O_V -TA (497 mV dec⁻¹) and S/TRA (454 mV dec⁻¹), and the Tafel slope from the reduction peak (Fig. 3i) for S/ O_V -TRA (353 mV dec⁻¹) is inferior to those of S/ O_V -TA (688 mV dec⁻¹) and S/TRA (543 mV dec⁻¹), indicating that S/ O_V -TRA delivers enhanced reaction kinetics for polysulfides reduction and Na_2S oxidation.

Fig. 4 displays the electrochemical performance in RT Na–S batteries based on S/O_V-TRA, S/O_V-TA and S/TRA. Fig. 4a exhibits the CV tests of S/O_V-TRA for the initial four cycles at 0.1 mV s⁻¹. The cathodic peak at 1.73 V in the initial curve was observed, which is attributed to the conversion of S₈ to Na₂S_x (4 ≤ x ≤ 8).^{55–57} The cathodic peak at 0.77 V is mainly attributed to the conversion of Na₂S_x (4 ≤ x ≤ 8) to Na₂S₂ and Na₂S, the formation of the surface SEI film, and the occurrence of side reactions during the initial discharge process.^{55–57} In the subsequent cycles, the CV profiles display two cathodic peaks at 1.60 and 1.02 V and two anodic peaks at 1.85 and 2.18 V, which are attributed to the conversion of long-chain NaPSs to Na₂S₄ and eventually into Na₂S and the reversible oxidation of Na₂S₄ to NaPSs and then to S₈.²⁹ Additionally, the following CV curves are similar in shape, suggesting that S/O_V-TRA possesses excellent cyclic stability and favorable reversibility. The CV profiles of S/O_V-TA and S/TRA (Fig. S16†) exhibit similar electrochemical processes to S/O_V-TRA. Fig. 4b illustrates the

second charge/discharge curves, where S/O_V-TRA exhibits a higher capacity (920 mA h g⁻¹) and a smaller voltage gap (0.53 V), compared to S/O_V-TA (430 mA h g⁻¹, 0.96 V) and S/TRA (536 mA h g⁻¹, 0.80 V), further demonstrating that the rich oxygen vacancies possess superior electrocatalytic activity toward NaPSs for RT Na–S batteries. Furthermore, as shown in Fig. 4c, the cycling performance of S/O_V-TRA exhibits a superior capacity of 870 mA h g⁻¹ at 0.1 C (1 C = 1675 mA h g⁻¹) with a capacity retention of 94.5% after 100 cycles. However, the capacities of S/O_V-TA and S/TRA are 279 mA h g⁻¹ and 454 mA h g⁻¹ after 100 cycles, respectively. Additionally, the charge–discharge profiles of S/O_V-TRA at different cycles further demonstrate the good reversibility (Fig. 4d). Hence, it is inferred that O_V-TRA greatly diminishes the shuttle effect of NaPSs, minimizes the volume expansion, and fosters the prompt conversion of NaPSs. The rate performances of S/O_V-TRA, S/O_V-TA and S/TRA were evaluated in the range of 0.1 to 3 C (Fig. 4e). S/O_V-TRA exhibits excellent rate capability with

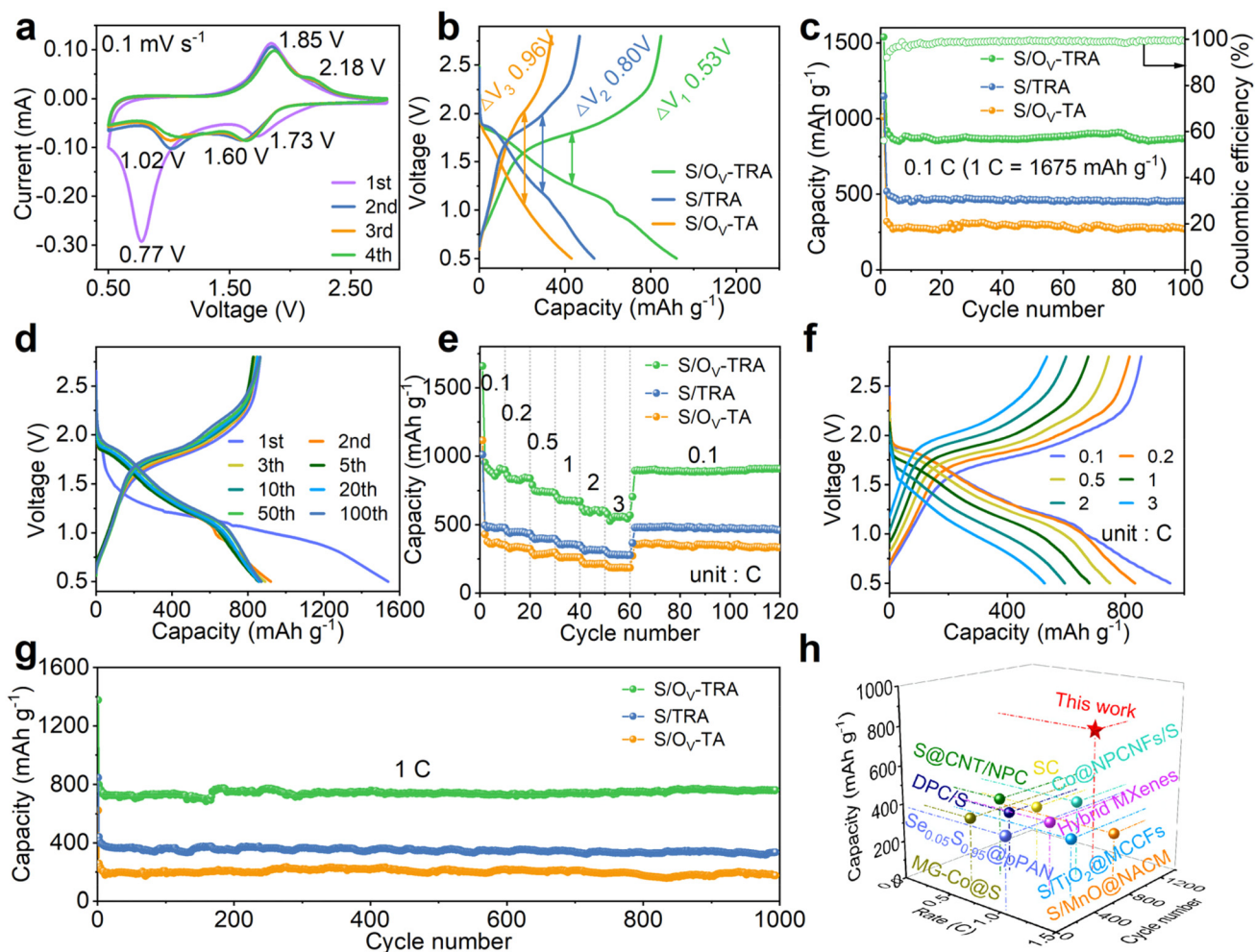


Fig. 4 (a) CV curves of S/O_V-TRA. (b) Charge–discharge profiles of S/O_V-TRA at 0.1 C. (c) Cycling performance at 0.1 C. (d) Charge–discharge profiles of S/O_V-TRA at 1 C. (e) The rate capabilities under various current densities. (f) Charge–discharge profiles of S/O_V-TRA at rates from 0.1 to 3 C. (g) Long-term cycling performance at 1 C. (h) Comparison of the long-term cycling performance with most previously S cathodes on the market for RT Na–S batteries.

capacities of 900, 838, 730, 673, 600, and 570 mA h g⁻¹ at 0.1, 0.2, 0.5, 1, 2, and 3 C, respectively, which is superior to those of S/O_V-TA and S/TRA. Fig. 4f still shows obvious charge–discharge plateau for S/O_V-TRA at different rates, suggesting the enhanced sulfur redox kinetics. Fig. 4g shows the cycling performance at 1 C after 1000 cycles, and S/O_V-TRA maintains a higher capacity of 759 mA h g⁻¹ with a capacity retention of 95.0% in comparison with those of S/O_V-TA (172 mA h g⁻¹, 66.4%) and S/TRA (326 mA h g⁻¹, 73.9%). Importantly, the electrochemical performance of S/O_V-TRA is superior to that of most previously reported S cathodes for RT Na–S batteries (Fig. 4h and Table S3†). This excellent performance emphasizes the crucial role of the homojunction structure containing abundant oxygen vacancies in boosting the catalytic conversion of NaPSs, thereby contributing to outstanding electrochemical performance.

The CV curves of S/O_V-TRA with various scan rates are arranged to further investigate the kinetic process (Fig. S17†). The b values for redox peaks are 0.81 and 0.99, suggesting the fast reaction kinetics for S/O_V-TRA. As the scan rate increases, the influence of capacitive charge becomes more pronounced, where the contribution ratio of capacitive at 1.0 mV s⁻¹ is approximately 79% (Fig. S17c and d†), which is higher than those of S/O_V-TA (39%) (Fig. S18†) and S/TRA (64%) (Fig. S19†). These results confirm that the oxygen vacancy can significantly enhance Na⁺ storage kinetics and expand the electrocatalytic efficiency of NaPSs.⁵⁸ Na⁺ diffusion coefficients were evaluated using the galvanostatic intermittent titration technique (GITT) to reflect the reaction kinetics of polysulfides transformation (Fig. 5a and S20†), where the Na⁺ diffusion coefficients of S/O_V-TRA are even higher than those of S/O_V-TA and S/TRA during the whole process. Fig. 5b demonstrates the equivalent

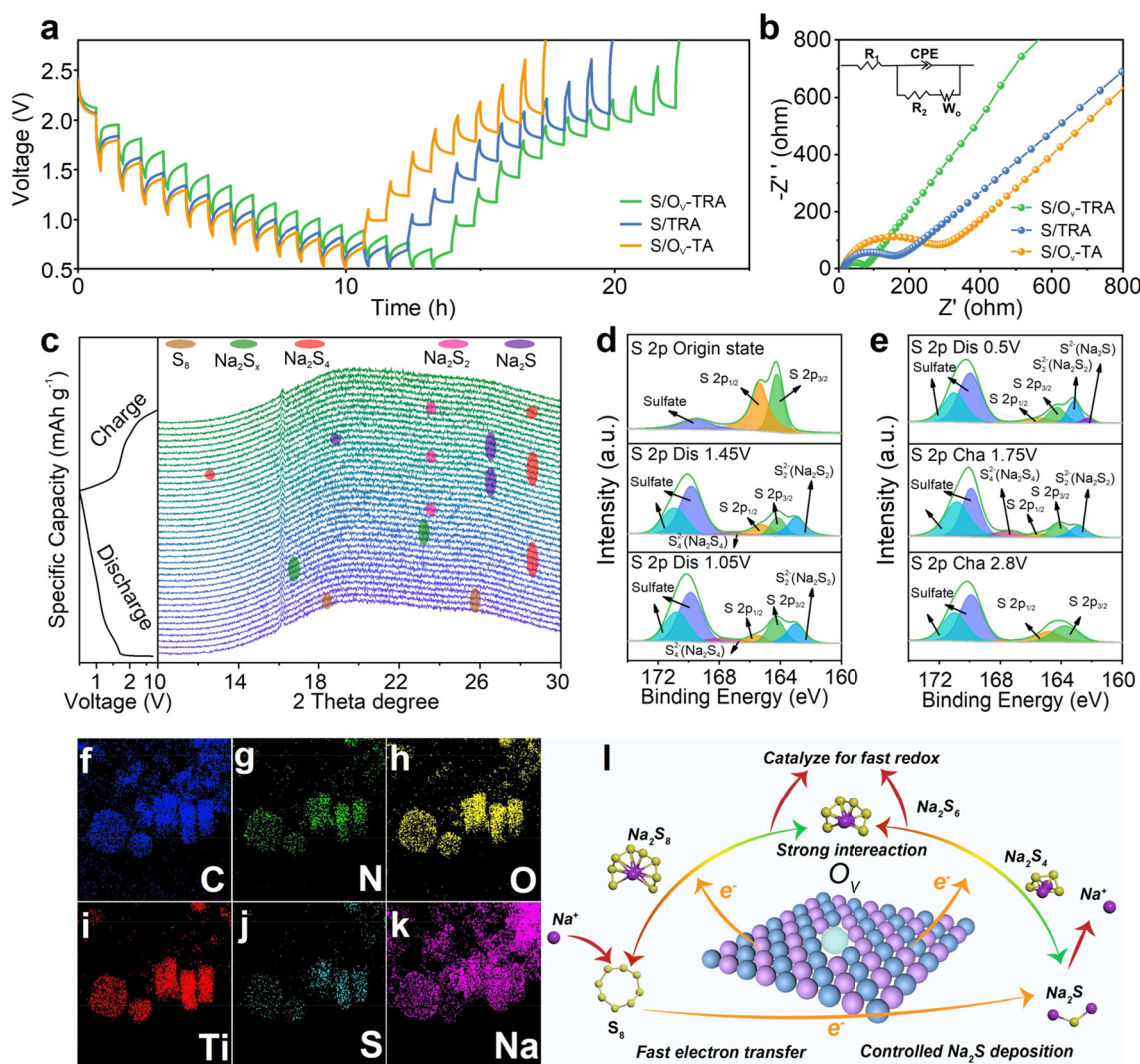


Fig. 5 (a) GITT profiles and (b) EIS plots of S/O_V-TRA, S/O_V-TA, and S/TRA. (c) *In situ* XRD patterns and (d) and (e) *ex situ* XPS spectrum of the S/O_V-TRA cathode at different discharge/charge states for RT Na–S batteries. (f–k) Elements mapping images of S/O_V-TRA after cycling. (l) Schematic for the acceleration of O_V-TRA on the polysulfides conversion in RT Na–S batteries.

circuits corresponding to the Nyquist plots. Besides, S/O_V-TRA (60 Ω) has a smaller charge transfer resistance (R_{ct}) than S/O_V-TA (260 Ω) and S/TRA (143.5 Ω) (Fig. 5b). Fig. S21† exhibits the resistance after cycles, where the R_{ct} of S/O_V-TRA gradually decreases due to the generation of a more stable surface SEI film after repeated cycles.⁵⁹ The electrochemical mechanism of the cycling process was studied by *in situ* XRD (Fig. 5c). The peaks of S₈ gradually disappear, and the peaks of Na₂S_x ($4 \leq x \leq 8$) are present in the initial cathodic cycle. With continuous discharge, the characteristic peak of Na₂S₄ was observed, and the characteristic peak of Na₂S₂ appears at ≈0.8 V. Then, the characteristic peak of Na₂S is present when the discharge is sustained to about 0.7 V, demonstrating that the conversion from S₈ into Na₂S is completed. Besides, the extremely reversible process is displayed in the anodic cycle, where Na₂S gradually converts into Na₂S₄ and further into long-chain NaPSs. Furthermore, the *ex situ* XPS of S/O_V-TRA was also performed to elucidate the corresponding reversible processes (Fig. 5d and e). The S 2p XPS spectrum was fitted to two main peaks of S 2p_{1/2} and S 2p_{3/2} in the initial state.⁶⁰ Two peaks of Na₂S₄ (167.12 eV) and Na₂S₂ (162.91 eV) appeared at 1.45 V, demonstrating the formation of NaPSs.^{30,61} With discharge to 1.05 V, the peak intensity of Na₂S₄ gradually weakens, and the peak intensity of Na₂S₂ increases.³⁰ Upon discharge to 0.5 V, the peak of Na₂S was present at 162.18 eV. During the charge process, Na₂S was progressively reverted into Na₂S₂, Na₂S₄, and long-chain NaPSs, confirming the reversible charge–discharge process.⁶² Besides, according to the TEM observation, S/O_V-TRA exhibits excellent structural integrity after several cycles (Fig. 5f–k and Fig. S22†). These results manifest that O_V-TRA is effective for the adsorption and conversion of polysulfides (Fig. 5l), thus inhibiting the shuttle effect and boosting the reaction kinetics.

3. Conclusions

In general, TiO₂ homojunction with abundant oxygen vacancies was successfully prepared as the S host material for RT Na–S batteries. The designed anatase-rutile TiO₂ homojunction contributes to increased defect density in lattice and optimizes the electronic structure, which promotes the effective adsorption toward NaPSs and catalyzes the rapid transformation, thereby accelerating the reaction kinetics and improving the electrochemical performance of RT Na–S batteries. S/O_V-TRA displays a high capacity of 870 mA h g^{−1} at 0.1 C after 100 cycles, and a prominent cycle life with a high reversible capacity of 759 mA h g^{−1} at 1 C over 1000 cycles. This research provides a viable interfacial defect engineering strategy to promote the application of metal oxides in RT Na–S batteries.

Conflicts of interest

The authors declare no conflict of interest.

Acknowledgements

This work was supported by the National Key R&D Program of China (Grant No. 2021YFA1600202), the National Natural Science Foundation of China (21972145, 52172172, 22102169, 52302159), Natural Science Foundation of Anhui Province (2108085MB57), and the Scholar Program for the Outstanding Innovative Talent of College Discipline (Specialty) (gxbjZD2022005).

References

- 1 Y. Liu, F. Bettels, Z. Lin, Z. Li, Y. Shao, F. Ding, S. Liu and L. Zhang, *Adv. Funct. Mater.*, 2023, 2302626.
- 2 Y. Lei, H. Liu, Z. Yang, L. Zhao, W. Lai, M. Chen, H. Liu, S. Dou and Y. Wang, *Adv. Funct. Mater.*, 2023, 33, 2212600.
- 3 X. L. Huang, Y. X. Wang, S. L. Chou, S. X. Dou and Z. M. Wang, *Energy Environ. Sci.*, 2021, 14, 3757.
- 4 X. Zheng, Z. Gu, J. Fu, H. Wang, X. Ye, L. Huang, X. Liu, X. Wu, W. Luo and Y. Huang, *Energy Environ. Sci.*, 2021, 14, 4936.
- 5 J. Yang, Y. Zhai, X. Zhang, E. Zhang, H. Wang, X. Liu, F. Xu and S. Kaskel, *Adv. Energy Mater.*, 2021, 11, 2100856.
- 6 S. Zhang, Y. Yao and Y. Yu, *ACS Energy Lett.*, 2021, 6, 529.
- 7 Y. Wang, D. Zhou, V. Palomares, D. Shanmukaraj, B. Sun, X. Tang, C. Wang, M. Armand, T. Rojo and G. Wang, *Energy Environ. Sci.*, 2020, 13, 3848.
- 8 X. Hong, J. Mei, L. Wen, Y. Tong, A. J. Vasileff, L. Wang, J. Liang, Z. Sun and S. X. Dou, *Adv. Mater.*, 2019, 31, 1802822.
- 9 Y. Dai, C. Xu, X. Liu, X. He, Z. Yang, W. Lai, L. Li, Y. Qiao and S. Chou, *Carbon Energy*, 2021, 3, 253.
- 10 J. Zhou, Y. Yang, Y. Zhang, S. Duan, X. Zhou, W. Sun and S. Xu, *Angew. Chem., Int. Ed.*, 2021, 60, 10129.
- 11 S. Xin, L. Gu, N. H. Zhao, Y. X. Yin, L. J. Zhou, Y. G. Guo and L. J. Wan, *J. Am. Chem. Soc.*, 2012, 134, 18510.
- 12 Z. Li, H. B. Wu and X. W. (David) Lou, *Energy Environ. Sci.*, 2016, 9, 3061.
- 13 Z. Yan, J. Xiao, W. Lai, L. Wang, F. Gebert, Y. Wang, Q. Gu, H. Liu, S. L. Chou, H. Liu and S. X. Dou, *Nat. Commun.*, 2019, 10, 4793.
- 14 H. Hao, Y. Wang, N. Katyal, G. Yang, H. Dong, P. Liu, S. Hwang, J. Mantha, G. Henkelman, Y. Xu, J. A. Boscoboinik, J. Nanda and D. Mitlin, *Adv. Mater.*, 2022, 34, 2106572.
- 15 C. Wu, W. Lai, X. Cai, S. Chou, H. Liu, Y. Wang and S. Dou, *Small*, 2021, 17, 2006504.
- 16 Z. Yan, Y. Liang, W. Hua, X. G. Zhang, W. Lai, Z. Hu, W. Wang, J. Peng, S. Indris, Y. Wang, S. L. Chou, H. Liu and S. X. Dou, *ACS Nano*, 2020, 14, 10284.
- 17 Z. F. Huang, P. Jaumaux, B. Sun, X. Guo, D. Zhou, D. Shanmukaraj, M. Armand, T. Rojo and G. Wang, *Electrochem. Energy Rev.*, 2023, 6, 21.
- 18 C. Wu, Y. Lei, L. Simonelli, D. Tonti, A. Black, X. Lu, W. Lai, X. Cai, Y. Wang, Q. Gu, S. Chou, H. Liu, G. Wang and S. Dou, *Adv. Mater.*, 2022, 34, 2108363.

- 19 Y. Liu, S. Ma, M. Rosebrock, P. Rusch, Y. Barnscheidt, C. Wu, P. Nan, F. Bettels, Z. Lin, T. Li, B. Ge, N. C. Bigall, H. Pfnür, F. Ding, C. Zhang and L. Zhang, *Adv. Sci.*, 2022, **9**, 2105544.
- 20 H. Zhang, L. K. Ono, G. Tong, Y. Liu and Y. Qi, *Nat. Commun.*, 2021, **12**, 4738.
- 21 X. L. Huang, X. Zhang, L. Zhou, Z. Guo, H. K. Liu, S. X. Dou and Z. Wang, *Adv. Sci.*, 2023, **10**, 2206558.
- 22 N. Wang, Y. Wang, Z. Bai, Z. Fang, X. Zhang, Z. Xu, Y. Ding, X. Xu, Y. Du, S. Dou and G. Yu, *Energy Environ. Sci.*, 2020, **13**, 562.
- 23 W. Bao, C. E. Shuck, W. Zhang, X. Guo, Y. Gogotsi and G. Wang, *ACS Nano*, 2019, **13**, 11500.
- 24 G. Yao, Z. Li, Y. Zhang, Y. Xiao, L. Wei, H. Niu, Q. Chen, Y. Yang and F. Zheng, *Adv. Funct. Mater.*, 2024, **34**, 2214353.
- 25 Y. Li, C. Wang, W. Wang, A. Y. S. Eng, M. Wan, L. Fu, E. Mao, G. Li, J. Tang, Z. W. Seh and Y. Sun, *ACS Nano*, 2020, **14**, 1148.
- 26 D. Fang, S. Huang, T. Xu, P. Sun, X. L. Li, Y. V. Lim, D. Yan, Y. Shang, B. J. Su, J. Y. Juang, Q. Ge and H. Y. Yang, *ACS Appl. Mater. Interfaces*, 2023, **15**, 26650.
- 27 J. J. Wang, G. Q. Cao, R. X. Duan, X. Li and X. Li, *Acta Phys. - Chim. Sin.*, 2023, 2212005.
- 28 G. Q. Cao, R. X. Duan and X. F. Li, *EnergyChem*, 2023, **5**, 100096.
- 29 E. Zhang, X. Hu, L. Meng, M. Qiu, J. Chen, Y. Liu, G. Liu, Z. Zhuang, X. Zheng, L. Zheng, Y. Wang, W. Tang, Z. Lu, J. Zhang, Z. Wen, D. Wang and Y. Li, *J. Am. Chem. Soc.*, 2022, **144**, 18995.
- 30 J. Mou, Y. Li, L. Ou and J. Huang, *Energy Storage Mater.*, 2022, **52**, 111.
- 31 D. Fang, G. Wang, S. Huang, T. Chen Li, J. Yu, D. Xiong, D. Yan, X. Liang Li, J. Zhang, Y. Von Lim, S. A. Yang and H. Y. Yang, *Chem. Eng. J.*, 2021, **411**, 128546.
- 32 H. Zhang, L. Yang, P. Zhang, C. Lu, D. Sha, B. Yan, W. He, M. Zhou, W. Zhang, L. Pan and Z. Sun, *Adv. Mater.*, 2021, **33**, 2008447.
- 33 K. Zou, X. Chen, W. Jing, X. Dai, P. Wang, Y. Liu, R. Qiao, M. Shi, Y. Chen, J. Sun and Y. Liu, *Energy Storage Mater.*, 2022, **48**, 133.
- 34 H. Wang, Y. Wei, G. Wang, Y. Pu, L. Yuan, C. Liu, Q. Wang, Y. Zhang and H. Wu, *Adv. Sci.*, 2022, **9**, 2201823.
- 35 X. Guan, S. Zong and S. Shen, *Nano Res.*, 2022, **15**, 10171.
- 36 D. Q. Cai, J. L. Yang, T. Liu, S. X. Zhao and G. Cao, *Nano Energy*, 2021, **89**, 106452.
- 37 X. Gao, M. Wei, D. Ma, X. Yang, Y. Zhang, X. Zhou, L. Li, Y. Deng and W. Yang, *Adv. Funct. Mater.*, 2021, **31**, 2106700.
- 38 S. J. Phang, V. L. Wong, L. L. Tan and S. P. Chai, *Appl. Mater. Today*, 2020, **20**, 100741.
- 39 P. Xue, K. Zhu, W. Gong, J. Pu, X. Li, C. Guo, L. Wu, R. Wang, H. Li, J. Sun, G. Hong, Q. Zhang and Y. Yao, *Adv. Energy Mater.*, 2022, **12**, 2200308.
- 40 H. Raza, S. Y. Bai, J. Y. Cheng, S. Majumder, H. Zhu, Q. Liu, G. Zheng, X. Li and G. Chen, *Electrochem. Energy Rev.*, 2023, **6**, 29.
- 41 G. Liu, L. Xu, Y. Li, D. Guo, N. Wu, C. Yuan, A. Qin, A. Cao and X. Liu, *Chem. Eng. J.*, 2022, **430**, 132689.
- 42 Y. Yang, H. Wang, Q. Zhou, M. Kong, H. Ye and G. Yang, *Nanoscale*, 2013, **5**, 10267.
- 43 M. Ding, S. Fan, S. Huang, M. E. Pam, L. Guo, Y. Shi and H. Y. Yang, *ACS Appl. Energy Mater.*, 2019, **2**, 1812.
- 44 L. Ma, Y. Zhang, S. Zhang, L. Wang, C. Zhang, Y. Chen, Q. Wu, L. Chen, L. Zhou and W. Wei, *Adv. Funct. Mater.*, 2023, **33**, 2305788.
- 45 H. Li, C. Chen, Y. Yan, T. Yan, C. Cheng, D. Sun and L. Zhang, *Adv. Mater.*, 2021, **33**, 2105067.
- 46 X. Hu, J. Wang, J. Wang, Y. Deng, H. Zhang, T. Xu and W. Wang, *Appl. Catal., B*, 2022, **318**, 121879.
- 47 M. Li, P. Wang, Z. Ji, Z. Zhou, Y. Xia, Y. Li and S. Zhan, *Appl. Catal., B*, 2021, **289**, 120020.
- 48 C. Yi, J. Huo and Z. Liu, *Chem. Eng. J.*, 2023, **467**, 143541.
- 49 X. Tang, A. Yu, Q. Yang, H. Yuan, Z. Wang, J. Xie, L. Zhou, Y. Guo, D. Ma and S. Dai, *J. Am. Chem. Soc.*, 2024, **146**, 3764.
- 50 J. Li, G. Hu, R. Yu, X. Liao, K. Zhao, T. Li, J. Zhu, Q. Chen, D. Su, Y. Ren, K. Amine, L. Mai, L. Zhou and J. Lu, *ACS Nano*, 2023, **17**, 21604.
- 51 Y. Zou, Y. Hu, A. Uhrich, Z. Shen, B. Peng, Z. Ji, M. Muhler, G. Zhao, X. Wang and X. Xu, *Appl. Catal., B*, 2021, **298**, 120584.
- 52 Z. Li, C. Zhou, J. Hua, X. Hong, C. Sun, H. Li, X. Xu and L. Mai, *Adv. Mater.*, 2020, **32**, 1907444.
- 53 H. Shao, W. Wang, H. Zhang, A. Wang, X. Chen and Y. Huang, *J. Power Sources*, 2018, **378**, 537.
- 54 Y. Wang, Y. Xiong, Q. Huang, Z. Bi, Z. Zhang, Z. Guo, X. Wang and T. Mei, *J. Mater. Chem. A*, 2022, **10**, 18866.
- 55 F. Zheng, Y. Zhang, G. Ding, Y. Xiao, L. Wei, J. Su, C. Wang, Q. Chen and H. Wang, *Adv. Funct. Mater.*, 2024, **34**, 2310598.
- 56 X. Ye, J. Ruan, Y. Pang, J. Yang, Y. Liu, Y. Huang and S. Zheng, *ACS Nano*, 2021, **15**, 5639.
- 57 D. Ma, Y. Li, J. Yang, H. Mi, S. Luo, L. Deng, C. Yan, M. Rauf, P. Zhang, X. Sun, X. Ren, J. Li and H. Zhang, *Adv. Funct. Mater.*, 2018, **28**, 1705537.
- 58 J. Liu, J. Wang, L. Zhu, X. Chen, Q. Ma, L. Wang, X. Wang and W. Yan, *Chem. Eng. J.*, 2021, **411**, 128540.
- 59 Y. Niu, M. Xu, C. Cheng, S. Bao, J. Hou, S. Liu, F. Yi, H. He and C. M. Li, *J. Mater. Chem. A*, 2015, **3**, 17224.
- 60 S. Zhang, Y. Yao, X. Jiao, M. Ma, H. Huang, X. Zhou, L. Wang, J. Bai and Y. Yu, *Adv. Mater.*, 2021, **33**, 2103846.
- 61 X. Zhou, Z. Yu, Y. Yao, Y. Jiang, X. Rui, J. Liu and Y. Yu, *Adv. Mater.*, 2022, **34**, 2200479.
- 62 Z. Q. Li, X. Chen, G. Yao, L. Wei, Q. Chen, Q. Luo, F. Zheng and H. Wang, *Adv. Funct. Mater.*, 2024, 2400859.